Photodetachment in a strong laser field: An experimental test of Keldysh-like theories

Boris Bergues, Zunaira Ansari,* Dag Hanstorp,† and Igor Yu. Kiyan
Physikalisches Institut, Albert-Ludwigs-Universität, D-79104 Freiburg, Germany
(Received 16 May 2007; published 20 June 2007)

We investigate the photodetachment process in the negative fluorine ion in a strong linearly polarized laser field. Angle-resolved momentum distributions of photoelectrons are measured with the use of an imaging technique for a wide range of laser frequencies and peak intensities. The nonmonotonic structure recorded in photoelectron spectra is interpreted in terms of the quantum interference effect predicted by a Keldysh-like theory. In particular, the dependence of the interference term on the laser parameters is used to explain the origin of the observed spectral features. Our results unambiguously show that the length gauge is the proper one to use in the frame of the strong-field approximation.

DOI: 10.1103/PhysRevA.75.063415 PACS number(s): 32.80.Rm, 32.80.Gc

I. INTRODUCTION

Atomic ionization in a strong laser field has received great attention during the last decades. A major step in the experimental study of this process came with the development of short-pulse lasers that can generate electromagnetic radiation of high peak intensity. The advancement in laser technology brought the unique chance not only to measure the total ionization yield, but also study the kinetic energy and angular distributions of the emitted electrons. Such experiments have already been reported in numerous publications [1]. Application of a short laser pulse of subpicosecond duration is crucial here in order to avoid distortions of electron distributions caused by the ponderomotive acceleration of photoelectrons from the laser focus [2].

Angle-resolved photoelectron spectra carry rich information necessary to reveal the mechanisms that govern the ionization process. In particular, in a linearly polarized laser field the rescattering mechanism is found to contribute to the emission of hot electrons with kinetic energies beyond the classical cutoff value of $2U_p$ [3,4], where U_p represents the ponderomotive energy of a free electron in the field. According to the rescattering model, the ejected electron is turned back to the residual core under the action of the external field, where it scatters elastically on the core potential and, eventually, leaves the atomic system. Electrons emitted in such a stepwise process are shown to compose a characteristic plateau in the angle-resolved energy spectrum, which extends over the energy range between $2U_p$ and $10U_p$ and is localized at small angles with respect to the laser polarization axis [5]. Thus, measurements of photoelectron distributions turned out to be crucial in the experimental identification of the rescattering effect.

Another fundamental effect that manifests itself in photoelectron spectra consists in the quantum interference of electron paths in the final continuum state. This effect can be understood in terms of the saddle-point analysis of the transition amplitude presented in Refs. [6] and [7] for the direct process of ionization and for the process that involves rescattering, respectively. The analysis reveals that within one field oscillation period the transition to the final state with a drift momentum **p** takes place preferentially at specific moments determined by the given vector **p**. For a linearly polarized laser field, there are two such distinct instants contributing to direct electron emission, while the rescattering process comprises several of them. Each such instant represents an origin of the electron path in the continuum and can be associated with a trajectory followed by the electron on its way out from the atomic core. The motion along different paths is coherent, which gives rise to the interference effect. The interference results in a nonmonotonic spectrum of photoelectrons. This effect has already been observed in our experiments on photodetachment of negative ions [8]. Its manifestation in electron spectra produced by the process of ionization with rescattering was reported in Refs. [9,10]. Below we discuss the interference effect in greater detail and in connection with our new experimental results. One task of the present work is to show the dependence of this effect on laser field parameters such as the frequency and the field strength.

Among numerous nonperturbative approaches to the problem of strong-field ionization, the Keldysh theory [11] received the greatest response. This theory has been under discussion during the last 40 years, and many authors have contributed to it [12–14]. The analytical character of this approach makes it rather practical for the identification of fundamental effects. In fact, the quantum interference effect introduced above is predicted by Keldysh-like theories (see Refs. [6] and [7] cited above). The Keldysh approach uses an approximation, also known as the strong-field approximation, where the core potential is neglected in the description of the continuum spectrum and the final electron state is represented by the Volkov wave function [15]. This assumption is justified when the core potential is of short range. Therefore, the Keldysh theory is well suited for negative ions, where the outer electron is bound by polarization forces and the long-range Coulomb potential is absent. This matter was already demonstrated in our previous experiments [8,16].

Because the Keldysh theory uses the strong-field approximation, its predictions are not independent of the gauge chosen to describe the electron interaction with the external

*Present address: Max Born Institute, D-12489 Berlin, Germany.
†Permanent address: Department of Physics, Göteborg University, SE-412 96 Göteborg, Sweden.

field. The gauge problem has been under discussion for a long time. Both the length and the velocity gauges have been used. For a circularly polarized field, the velocity gauge simplifies the calculation routine [14]. However, our recent experimental results are in favor of the length gauge [17]. Its validity follows also from the fact that in this gauge only are predictions consistent with the Wigner threshold law [18] in the limit of the small kinetic energies of photoelectrons [19,20]. For linear polarization, a few theoretical considerations also showed that the length gauge is the proper one. In particular, this was demonstrated in the frame of the quasistationary quasienergy state approach [21] and in the comparison of predictions by the strong-field approximation with a numerical solution of the time-dependent Schrödinger equation [22]. In the present work we prove the applicability of the length gauge experimentally.

II. EXPERIMENTAL PROCEDURE

In our experiment we investigate the process of electron photodetachment of the F^- ion exposed to a strong laser field of linear polarization. The experimental apparatus has been described before [19]. It consists of three differentially pumped vacuum sections. In the first section negative fluorine ions are extracted from a hollow cathode glow discharge created in a gas mixture of CF_4 and krypton. The ions are accelerated to a kinetic energy of 3 kV and mass selected in a Wien filter. The second section serves basically for the differential pumping. It contains some standard beam optics, such as an electrostatic lens and deflection plates, needed to optimize the passage of the ion beam through this section. In the third section the beam is bent by 90° in a quadrupole deflector in order to clean it from neutrals formed by collisional detachment with the residual gas molecules in the first and second sections. The beam is finally focused to a waist of 0.4 mm size in ultrahigh vacuum where it intersects the laser beam. Differential pumping allows us to maintain the interaction chamber at 4×10^{-10} mbar during the experiment. A typical ion current of F^- is 100 nA, as measured with a Faraday cup after the interaction region. Under these conditions the density of negative ions at the beam waist is approximately one order of magnitude higher than the density of the residual gas.

Linearly polarized infrared laser pulses are generated in an optical parametric amplifier (OPA) pumped with a mode-locked Ti:sapphire laser system at a 1-kHz repetition rate. A typical pulse energy delivered to the interaction chamber is of the order of 100 μJ. The laser beam is focused with a 15-cm-focal-length lens into the interaction region and crosses the ion beam at 90°. A typical focus size of 50 μm [full width at half maximum (FWHM)] with a Rayleigh range of 2.5 mm and a typical pulse length of 100 fs (FWHM) are measured with the use of our homebuilt tools for beam diagnostic. With these parameters the peak intensity in the interaction region is of the order of 10^{13} W/cm^2. Note that the Rayleigh length is much larger than the spot size of the focused ion beam, while the latter is much larger than the focus size of the laser beam. This intersection geometry of two beams is taken into account below in simulations of experimental spectra.

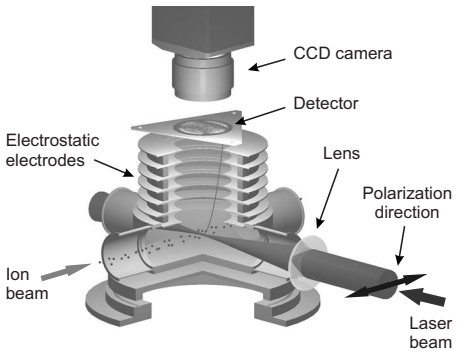

FIG. 1. Schematic view of the electron imaging spectrometer. Details are given in the text.

Electrons emitted in the process of photodetachment are detected with the use of an electron imaging spectrometer (EIS). The imaging technique allows us to record photoelectron distributions resolved simultaneously on both the angular and momentum scales. The EIS design is shown in Fig. 1. A set of electrodes creates an electrostatic field that accelerates the photoelectrons produced in the laser focus and projects them onto a position-sensitive detector. The detector consists of a pair of multichannel plates (MCPs) with a phosphor screen mounted behind. An electron arriving at the detector gives rise to a pulse of light on the phosphor screen at the impact position. A charge-coupled-device (CCD) camera records all light pulses during its exposure time, and a frame grabber stores their position coordinates in computer memory. Ideally, all electrons emitted with the same momentum vector should be projected onto the same point on the detector. A detailed discussion of the reduction of image distortions caused by the finite extension of the interaction region, the motion of the target ions, and the finite projection time is given in our earlier publication [19]. As in previous experiments, we reduce the image distortions by using hard projection in the velocity mapping regime [23].

A significant reduction of the electron background due to collisional detachment with residual gas molecules is achieved by gating the detector gain synchronously with the laser pulses for a time interval of 20 ns. This interval is long enough for emitted electrons to reach the detector. Another considerable improvement of the signal-to-noise ratio is achieved by breaking the signal and background acquisition in alternating sequences of 30 s duration, while subtracting background images from signal images.

The image processing involves a conventional Abel inversion routine based on the so-called "onion peeling" algorithm [24]. The strength of this algorithm consists in its parsimonious use of *a priori* knowledge about the physical process under investigation. In fact, the only assumption made by the algorithm in our case is the axial symmetry of the photodetachment process in a linearly polarized field. The routine requires the symmetry axis of the process to be parallel to the detector plane and the projection of an electron distribution onto the detector to be orthogonal (hard projection). The first requirement is fulfilled by turning the laser polarization direction parallel to the detector plane and the second requirement by the design of the EIS. The in-

verted image represents the angle-resolved momentum distribution of photoelectrons.

In order to investigate the sensitivity of the onion peeling algorithm to projection errors due to remaining image distortions in the spectrometer and to the statistical noise of raw images, we apply a Monte Carlo method to simulate a set of 3×10^6 electron trajectories with initial momenta randomly distributed according to theoretical electron distributions presented below. In these simulations we use the ion modeling software SIMION [25] to project electrons from the interaction region onto the detector plane while taking into account all details of the real EIS's geometry and the electrode potentials used in experiment, as well as the transversal velocity component of electrons due to the motion of the target negative ions. The simulated image is, in turn, inverted using the onion peeling algorithm. Except for a typical noise concentrated at the symmetry axis of the inverted image, no notable discrepancies are found between the reconstructed and initial electron distributions.

After the replacement of old MCPs we recalibrated our EIS following the procedure described in [16]. As was done before, we recorded the photoelectron spectra produced by one-photon detachment of H^- at different wavelengths. The laser intensities were kept low in order to avoid ponderomotive broadening of the energy peaks. We found the momentum scale of the detector to be linear with a velocity calibration coefficient of 0.9999×10^6 cm/s per pixel of the CCD camera. This value is very close to the old one. In addition, we used SIMION to confirm that the linearity of the scale extends to higher energies, up to 30 eV, which are not accessible by one-photon detachment in our setup. Kinetic energies of photoelectrons produced in the present experiment lie within this range. The detector response to a single-electron event is well described by a Gaussian function with a FWHM of 7 pixels.

III. RESULTS AND DISCUSSION

A. Experimental data

As formulated in the introductory section, one goal of the present work is to investigate the dependence of the quantum interference effect on the laser field parameters, such as the frequency ω and the peak intensity I_0. Since both parameters influence the character of the interference pattern, a systematic procedure suggests to keep one parameter fixed while varying the other. Practically, because the temporal and spatial shape of the laser pulse depends on the wavelength and optics alignment, it is easier to keep the wavelength constant and vary the peak intensity by attenuating the beam with the use of, e.g., thin neutral density filters. As an example, Fig. 2 shows the dependence of the photoelectron spectrum on the peak intensity at a wavelength of 1400 nm. At this wavelength at least four photons are needed to overcome the detachment threshold of F^-. Measurements are presented for the three intensity values of 7.7×10^{12} W/cm^2, 1.7×10^{13} W/cm^2, and 3.2×10^{13} W/cm^2, respectively. Each spectrum involves contributions from many excess photon detachment channels, which are not resolved due to ponderomotive broadening and partially due to the finite detector resolution.

The shown spectra reveal a nonmonotonic distribution over the energy and angular coordinates. In particular, apart from a maximum at lower kinetic energies each spectrum possesses a prominent second maximum on the laser polarization axis at higher energies. The second maximum is embraced by sidelobes, and the shape of each spectrum possesses a saddle between the two maxima. With the increase of the peak intensity, the positions of the saddle and of the second maximum move to higher kinetic energies while this structure becomes narrower on the angular scale.

B. Theoretical aspects

As we reported earlier [8,26], the nonmonotonic structure in photoelectron distributions represents a manifestation of the quantum interference effect. In order to discuss this effect in detail, we appeal here to the Keldysh-like theory by Gribakin and Kuchiev [6]. According to this theory, the adiabatic electron transition to the final state with a drift momentum vector $\mathbf{p}$ preferentially takes place when the condition

$$\frac{1}{2}\left(\mathbf{p}+\frac{\mathbf{F}}{\omega}\sin\omega t\right)^2=E_0 \tag{1}$$

is satisfied (atomic units, $e=m=\hbar=1$, are used throughout). Here $E_0=-\kappa^2/2$ is the energy of the initial bound state, $\mathbf{F}$ is the amplitude of the external electric field, $\mathbf{F}(t)=\mathbf{F}\cos\omega t$, and the term on the left-hand side of the equation represents the electron kinetic energy attributed to a superposition of the drift and the quiver motion. In the following we assume that the field polarization axis is parallel to the z axis of Cartesian coordinates.

Equation (1) has a fundamental meaning: it reflects the adiabatic character of the transition, where the energy of the final state matches the energy of the initial state at the transition instant. Apparently, one should search for solutions of Eq. (1) in the plane of complex time t. It has two pairs of complex conjugate roots in the interval $0\leqslant\mathrm{Re}(\omega t)<2\pi$. According to the general theory of adiabatic transitions [27], the two roots that lie in the upper half-plane of complex t have physical meaning and should be taken into account. Due to the fact that the transition takes place at two different instants of time within an oscillation period of the external field, the process of photodetachment acquires an interference character.

In the theory by Gribakin and Kuchiev, Eq. (1) appears as a saddle-point condition when evaluating the n-photon transition amplitude with the method of steepest descents [6]:

$$A_{\mathbf{p}n}=\frac{1}{T}\int_0^T\left[E_0-\frac{(\mathbf{p}+\mathbf{k}_t)^2}{2}\right]\Phi_0(\mathbf{p}+\mathbf{k}_t)e^{iS(\omega t)}dt, \tag{2}$$

where T is the oscillation period of the laser field, $\Phi_0(\mathbf{q})$ is the Fourier transform of the initial wave function $\Psi_0(\mathbf{r})$, $\mathbf{k}_t=(\mathbf{F}/\omega)\sin\omega t$ is the momentum of the quiver motion, and

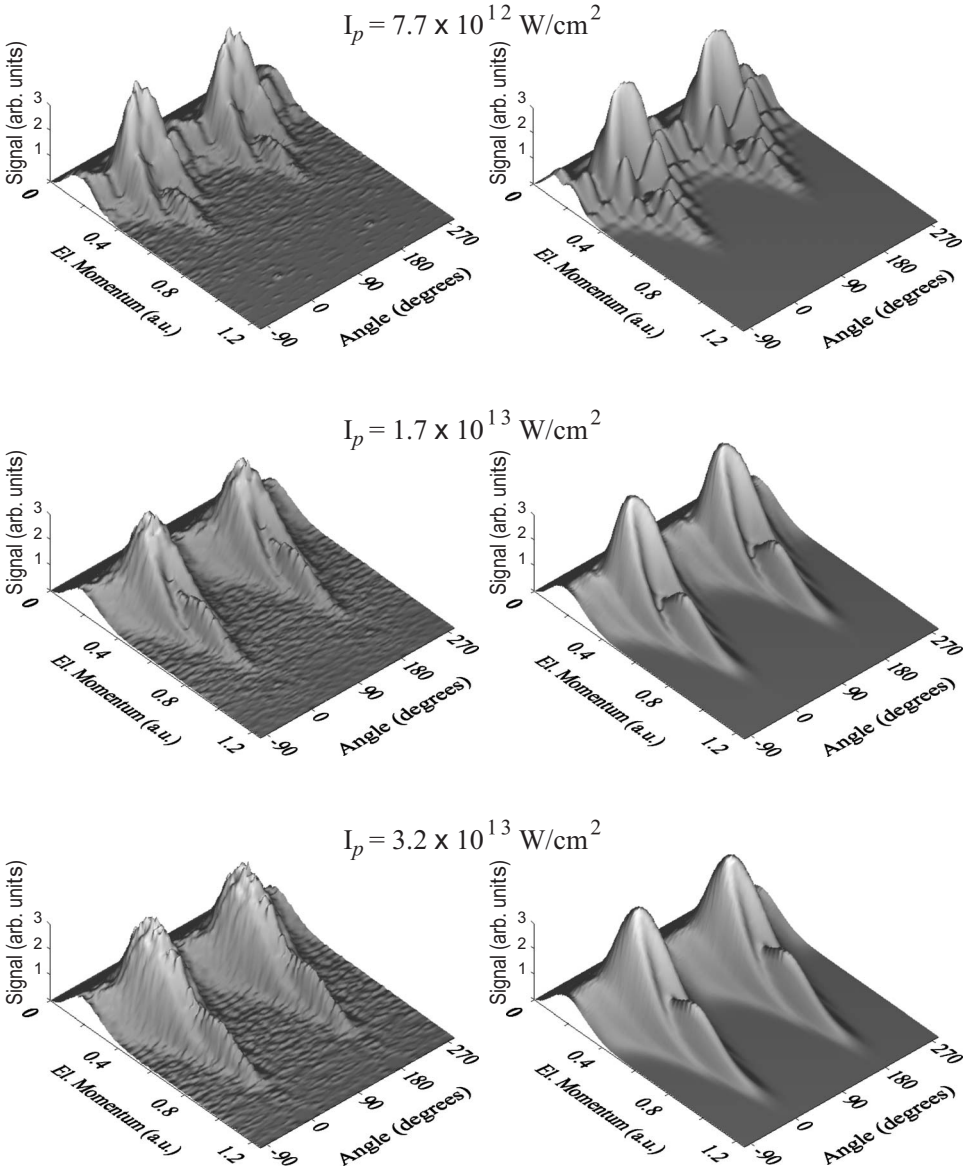

FIG. 2. Angle-resolved momentum distributions of photoelectrons produced by photodetachment of F^- in a laser field of 1400 nm wavelength. Results are obtained for the three given values of the peak intensity I_p. Experimental data are presented on the left-hand side. Spectra simulated with the use of the Keldysh-like theory [6] are shown on the right-hand side.

$$S(\omega t) = \frac{1}{2}\int^{t} (\mathbf{p} + \mathbf{k}_{t'})^2 dt' - E_0 t \tag{3}$$

represents the coordinate-independent part of the classical action. The method of steepest descents is applicable here because $S(\omega t) \sim 2\pi n$ and the integrand of Eq. (2) contains a rapidly oscillating exponent when the number of absorbed photons is large, $n \gg 1$.

The explicit form of the action (3) is

$$S(\phi) = n\phi - \xi \cos\phi - \frac{z}{2}\sin 2\phi, \tag{4}$$

where $\phi = \omega t$, $\xi = \mathbf{F}\cdot\mathbf{p}/\omega^2$, $z = U_p/\omega$, and $U_p = F^2/(4\omega^2)$ is the ponderomotive energy in a linearly polarized laser field. Analyzing the saddle-point condition $S' = 0$, one can find that two roots of this equation that lie in the upper half-plane of complex t have the same imaginary part value, $\mathrm{Im}(t_1) = \mathrm{Im}(t_2)$, while their real parts lie symmetrically with respect to the point where the field amplitude crosses zero. The crossing point $T/4$ or $3T/4$ should be chosen when the emission is considered towards the positive or negative z direction, respectively (see Fig. 3 for a schematic illustration). Taking this result into account, one can easily derive that the action S evaluated at the two saddle points has the following properties:

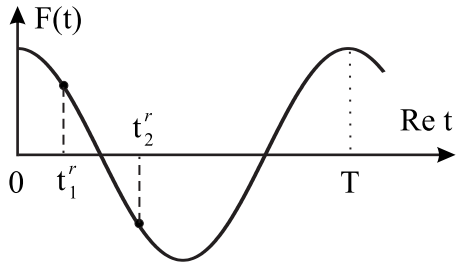

FIG. 3. Emission towards the positive z direction is represented by two saddle points with their real parts t_1^r and t_2^r, respectively. They lie symmetrically with respect to the point $T/4$ where the field amplitude $\mathbf{F}(t) = \mathbf{F}\cos(\omega t)$ crosses zero.

$$\mathrm{Im}(S_{t_1}) = \mathrm{Im}(S_{t_2}), \quad \mathrm{Re}(S_{t_1}) = n\pi - \mathrm{Re}(S_{t_2}),$$

$$S''_{t_1} = S''^{*}_{t_2}, \tag{5}$$

where S'' denotes the second derivative of the action. Then, the n-photon differential detachment rate, defined by a squared sum of two saddle-point contributions to the transition amplitude (2), can be represented as

$$\frac{dw_n}{d\Omega} = \frac{pC^2}{4\pi}(2\ell+1)\frac{(\ell-|m|)!}{(\ell+|m|)!}|P_\ell^{|m|}(\sqrt{1+p^2\sin^2\theta/\kappa^2})|^2 \times \frac{e^{-2a}}{\sqrt{|S''_{t_1}|}}[1+(-1)^{\ell+m}\cos(b-\beta)], \tag{6}$$

where $a=\mathrm{Im}(S_{t_1})$, $b=S_{t_1}-S_{t_2}$, $\beta=\arg(S''_{t_1})$, $P_\ell^{|m|}$ is the Legendre polynomial, (ℓ,m) are the angular momentum quantum numbers of the electron in the initial state, θ is the emission angle with respect to the polarization axis, and $p=(2n\omega-2U_p+2E_0)^{1/2}$ is the photoelectron momentum determined by the energy conservation. In the derivation of Eq. (6) we used the results of Ref. [6]. In particular, the sign term $(-1)^{\ell+m}$ in front of the cosine function results from evaluation of the Fourier transform of the initial-state wave function represented by its asymptotic form

$$\Psi_0^{\mathrm{A}}(\mathbf{r}) = C\frac{e^{-\kappa r}}{r}Y_{\ell m}(\hat{\mathbf{r}}), \tag{7}$$

where $C=0.7$ is a normalization coefficient. An explicit expression for the saddle points can also be found in Ref. [6].

C. Interference effect

The term in square brackets in Eq. (6) represents the interference term. As a function of p and θ, it varies rapidly between 0 and 2. The rest of Eq. (6) represents a smoothly varying function of p and θ, and we can consider it as an amplitude factor in front of the interference term. The amplitude factor describes a single saddle-point contribution to the photodetachment rate and is the same for both saddle points. As an illustration, Fig. 4 shows the contribution of the 11-photon detachment channel to the spectrum obtained at the 3.2×10^{13} W/cm^2 peak intensity (the bottom spectrum in Fig. 2). The top part of Fig. 4 represents results of simulations where only one saddle point is considered. The shape of this spectrum is rather smooth. It becomes strongly modulated when the interference term is taken into account (see the bottom part of the figure). We should notice here that the continuity of spectra along the momentum coordinate is due to the ponderomotive shift and is caused by the intensity distribution in the laser focus. More details on the simulation routine will be given below.

In Fig. 5 we plot the amplitude and interference terms separately for a large number of channels above the detachment threshold. For the sake of illustration, the intensity distribution in this simulation is restricted to the range between the peak value of 3.2×10^{13} W/cm^2 and the value of 2.72×10^{13} W/cm^2. Within this range the change in the ponderomotive shift is limited to one-photon energy, so that neighboring channels do not overlap and can be well distinguished in the figure. For the same purpose, we consider only photodetachment from the $m=0$ component of the initial state of F^- and disregard the fine structure splitting of the ground state of the residual atom. The top part of Fig. 5 shows the amplitude term. Here small jumps appear at momenta where two adjacent channels join each other. At such momenta electrons are detached in an n-photon channel at the lowest intensity or in an $(n+1)$-photon channel at the highest intensity of the given range, respectively. Disregarding these small jumps, one can consider that the amplitude factor represents a monotonic function of p, θ, and n. In contrast, the interference term varies rather rapidly between 0 and 2 (see the bottom part of Fig. 5). It is interesting to note that variations along the momentum coordinate are more frequent at emission angles close to 90° with respect to the laser polarization axis. Here, from channel to channel, the interference term changes from its maximum to minimum and vice versa. Such a behavior of photodetachment channels has already been pointed out in [6] and explained on the basis of symmetry properties of the transition amplitude. At small emission angles, maxima and minima of channels compose a pattern of concave lines. Several channels need to be involved to reproduce a fragment of this pattern. The pattern is intensity dependent: simulations at lower intensities (not presented here) show that the lines move towards the origin of the momentum scale and disappear when they approach zero. Namely, with the decrease of intensity the number of lines is less and their shape is also slightly modified. Therefore, in

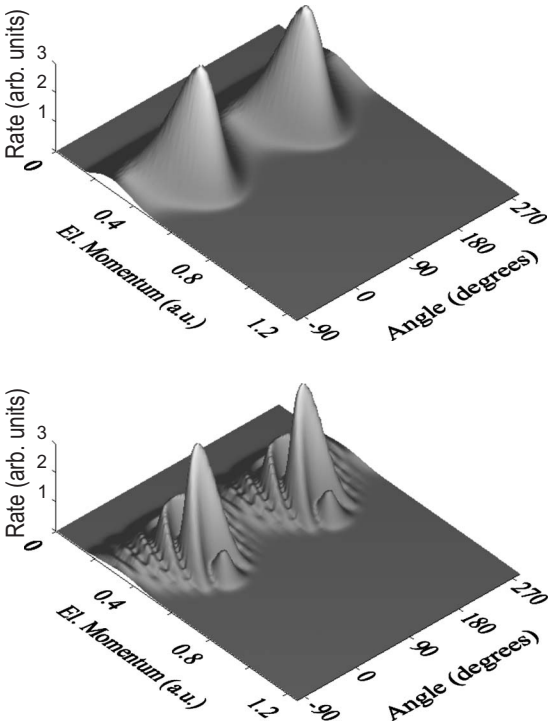

FIG. 4. Contribution of the 11-photon detachment channel to the spectrum shown at the bottom of Fig. 2 for the 3.2×10^{13} W/cm^2 peak intensity. The upper spectrum is simulated by taking a single saddle point into account. Simulations with two saddle points (the lower spectrum) reveal modulations due to the interference effect.

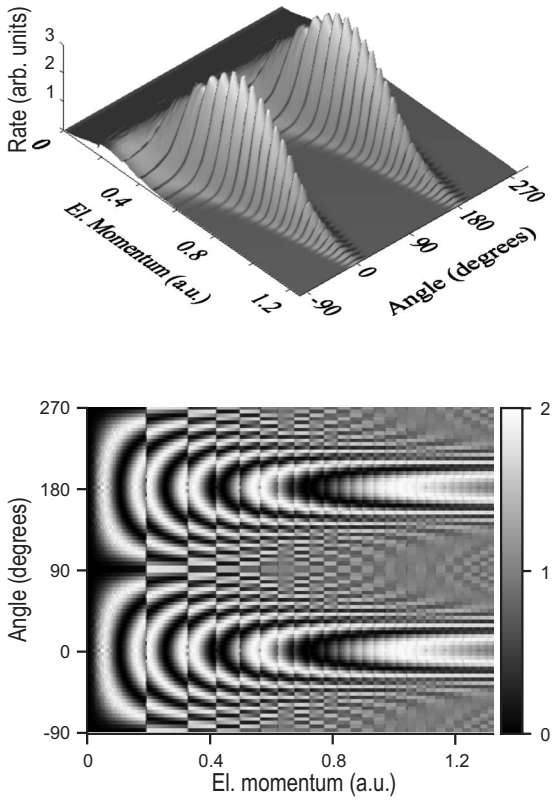

FIG. 5. The simulated amplitude (top) and interference (bottom) terms plotted for a large number of photodetachment channels and for a restricted range of intensities (given in the text). The channel of lowest order of nonlinearity is the ten-photon channel.

the experimental data the interference pattern shown in the simulation presented in Fig. 5 is, to a great extent, washed out due to the intensity distribution in the laser focus. Nevertheless, one can recognize that it is the concave structure in the interference term that gives rise to sidelobes present in the measured spectra. And it is the island apparent at small emission angles in the range of higher electron momenta ($p>0.8$ a.u.) that is responsible for the prominent second maximum at higher kinetic energies in the experimental data (see Fig. 2). Thus, the present discussion clearly demonstrates that the nonmonotonic structure in the experimentally measured spectra is caused by the interference effect.

Let us consider the interference term in Eq. (6) in greater detail. As was discussed in Refs. [6,28], in the limit of small photoelectron momenta the interference effect can be described by a geometrical phase difference between two de Broglie waves, emitted at the angle θ from two point sources at coordinates

$$\mathbf{r}_{1,2} = \pm \frac{\mathbf{F}}{\omega^2}\sqrt{1+\gamma^2},$$

where $\gamma=\kappa\omega/F$ is the Keldysh parameter of adiabaticity. The point sources lie symmetrically with respect to the core and are aligned along the polarization axis. It reflects the fact that in a linearly polarized field the electron release can take place equally at either side from the core. The coordinates $\mathbf{r}_{1,2}$ describe the electron position at two transition moments defined by the saddle points t_1 and t_2, respectively. Thus, in the limit of small momenta the process of photodetachment can be represented in terms of the double-slit interference. Following this discussion, we note that the difference in the action calculated at two saddle points can be represented as

$$S_{t_2} - S_{t_1} = \left(\frac{p^2}{2} - E_0\right)\Delta t + \mathbf{p}\cdot\Delta\mathbf{r} + \frac{1}{2}\int_{\mathbf{r}_1}^{\mathbf{r}_2}\mathbf{k}\cdot d\mathbf{r}, \qquad (8)$$

where $\Delta t=t_2-t_1\equiv \mathrm{Re}(t_2)-\mathrm{Re}(t_1)$, $\mathbf{k}$ is the quiver motion momentum introduced in Eq. (2), $\Delta\mathbf{r}=\mathbf{r}_2-\mathbf{r}_1$, and $\mathbf{r}_{1,2}=-(\mathbf{F}/\omega^2)\cos\omega t_{1,2}$ is the electron coordinate at transition moments t_1 and t_2, respectively. The middle term on the right-hand side of Eq. (8) represents the geometrical phase difference between two de Broglie waves discussed above. There are, however, additional terms that determine the interference character. In particular, the first term takes into account the phase shift of the initial and final states in the time interval Δt between the two transition moments. Apart from that, the third term describes the phase shift due to the source transformation from the coordinate $\mathbf{r}_1$ to coordinate $\mathbf{r}_2$. In the limit of small electron momenta p, the sum of the first and third terms is equal to $n\pi$. It results in the additional sign factor $(-1)^n$ in front of the cosine function in Eq. (6), while the interference effect acquires the character of double-slit interference. Strictly speaking, this discussion is valid when the term $\beta=\arg(S''_{t_1})$ can be neglected in Eq. (6). A simple analysis shows that β is negligible if one of the conditions $(p^2/2)\cos^2\theta \ll n\omega$ or $[n\omega-(p^2/2)\cos^2\theta]/n\omega \ll 1$ is satisfied. In particular, these conditions describe the limit of small momenta p, the case of electron emission in the direction perpendicular to the laser polarization, or the emission along the polarization axis with a high electron momentum.

D. Comparison of theory and experiment

In order to compare theory with experiment, two experimental circumstances need to be taken into account in simulations of photoelectron spectra. One of those, the spatial and temporal intensity distribution in the laser focus, has been already discussed above. It results in the ponderomotive energy broadening of detachment channels, and it leads to a washing out of the interference pattern. Another circumstance consists in the saturation of the photodetachment process—that is, the depletion of the primary negative ions during interaction with the laser pulse.

Since the Rayleigh range of the laser focus is much greater than the spot size of the focused ion beam, we can disregard the intensity variation along the propagation direction of the laser beam. Then, the spatiotemporal intensity distribution is described as a product of two Gaussian functions:

$$I(\rho,t) = I_p \exp\left(-\frac{\rho^2}{\sigma_\rho^2}\right)\exp\left(-\frac{t^2}{\sigma_t^2}\right), \qquad (9)$$

where I_p is the peak intensity, ρ is the radial coordinate in the plane perpendicular to the laser propagation direction, and the parameters σ_t and σ_ρ are obtained from the laser beam diagnostic.

For a given radial coordinate ρ and time t the n-photon yield of photoelectrons per unit time and unit volume of interaction is defined by the product of the detachment rate and the population of negative ions in the ground state. Since the valence electron in F^- has orbital momentum $\ell=1$, the detachment rate should be summed over contributions from the initial-state components with $m=0,\pm1$. In the simulations we also perform the statistical averaging of channels associated with the two different spin-orbit sublevels of the final atomic state, $^2P^0_{1/2}$ and $^2P^0_{3/2}$, respectively. These channels are characterized by different binding energies $|E_0|$. The binding energy of 3.401 189 eV assigned to the lower $^2P^0_{3/2}$ parent sublevel and the fine-structure splitting energy of 50.1 meV are taken from Ref. [29]. Thus, the averaged detachment rate is

$$\frac{d}{d\Omega}W_n(\theta,I(\rho,t)) = \sum_{m=-1}^{+1}\sum_j \frac{2j+1}{2L+1}\frac{dw_n^{(m,j)}}{d\Omega}, \tag{10}$$

where $j=\frac{1}{2},\frac{3}{2}$ are the two possible values of the total angular momentum of the residual atom, $L=1$ is its total orbital momentum, and $dw_n^{(m,j)}/d\Omega$ is the differential rate (6) calculated for a channel with given m and j. For the n-photon detachment yield per unit time and unit volume we have

$$y_n(\theta,\rho,t) = g(\rho,t)\frac{d}{d\Omega}W_n(\theta,I(\rho,t)). \tag{11}$$

Taking depletion into account, the ground-state population is

$$g(\rho,t) = g_0 \exp\left\{-\sum_n \int_{-\infty}^{t} d\tau\, W_n(I(\rho,\tau))\right\}, \tag{12}$$

where g_0 is the initial density of negative ions and W_n is the n-photon detachment rate integrated over the solid angle. A simulated photoelectron distribution over the momentum and angular coordinates is obtained by integrating Eq. (11) over the radius ρ and time t, and adding together contributions from different n-photon channels:

$$\frac{d\mathcal{N}}{d\Omega}(p,\theta) \propto \sum_n \int_0^\infty d\rho\,\rho \int_{-\infty}^{\infty} dt\, y_n(\theta,\rho,t) \times \delta\left(n\omega - \frac{p^2}{2} - \frac{I(\rho,t)}{4\omega^2} + E_0\right), \tag{13}$$

where the δ function accounts for energy conservation. As the last step of the routine, the electron distribution is convoluted with the measured response function of the detector to a single electron event.

Simulated spectra for the three experimental values of the peak intensity and wavelength of 1400 nm are presented on the right-hand side of Fig. 2. The figure demonstrates very good agreement between theory and experiment. One can see that all features of the nonmonotonic structure of each experimental spectrum are well reproduced in simulations. We found that the saturation effect plays an essential role when the peak intensity is 3.2×10^{13} W/cm^2, while this effect is negligible for a peak intensity of 7.7×10^{12} W/cm^2. At the middle peak intensity value saturation plays a minor role.

We should emphasize at this point that simulated spectra shown in Fig. 2 are obtained in the length gauge. Comparison of experiment with predictions in the velocity gauge will be presented below.

E. Wavelength dependence of the interference pattern

Numerous photoelectron spectra of F^- have been measured at different laser wavelengths in the range between 1200 nm and 1800 nm. The agreement between experimental results and predictions in the length gauge is found to be very good for each measurement. In these separate experiments, the laser output, the focus size, and the pulse width were dependent on the wavelength and the optics alignment and varied significantly from measurement to measurement. This prevented us from keeping the peak intensity in the interaction region at a constant level while tuning the wavelength. Therefore, for the sake of systematic presentation of the data, we show in Fig. 6 simulated spectra obtained at the given peak intensity value of 1.7×10^{13} W/cm^2. The spectra are calculated for four different wavelengths that cover the experimental range. The laser beam parameters used in simulations are the same as those attributed to the middle spectrum in Fig. 2.

One can see that with an increase of the wavelength the saddle lying between the sidelobes and the second highest energy peak move towards higher electron momenta, while the relative height of this peak becomes smaller. The lower-energy part of the spectrum also undergoes large modifications. Here the number of shoulders embracing the main peak increases with wavelength. In order to understand these results, we refer again to the representation of the photodetachment rate by the product of the amplitude and interference terms. Let us consider the electron emission along the laser polarization axis. In the limit of high kinetic energies $(p^2/2 \gg |E_0|, U_p)$ the differential rate (6) has the form [8]

$$\left.\frac{dw_n}{d\Omega}\right|_{\Theta=0} = \left(\frac{e^3U_p}{p^2}\right)^n\left[1+(-1)^\ell \sin\left(\frac{2}{3}\frac{\kappa^3}{\omega p}+\frac{\kappa}{p}\right)\right]. \tag{14}$$

Note that only the $m=0$ component of the ground state contributes to the emission at $\theta=0°$. The interference term in square brackets oscillates as a function of $1/p$. Its oscillation period on the momentum scale is defined by the energy of the initial state and the laser frequency and is independent of the laser intensity. For $\ell=1$, the first maximum of the interference term from the side of high electron momenta—that is, the one in the spectrum with the highest kinetic energy—appears at

$$p_m = \frac{2}{3\pi}\left(\frac{4|E_0|}{3\omega}+1\right)\kappa. \tag{15}$$

For instance, at a wavelength of 1400 nm and for the binding energy $|E_0|=3.401\,189$ eV of the ground state of F^-, the momentum (15) corresponds to a kinetic energy of approximately 5.7 eV. This value is close to the position of the maximum at 4.5 eV in the experimental data shown in next section. One should also take into account that the maximum

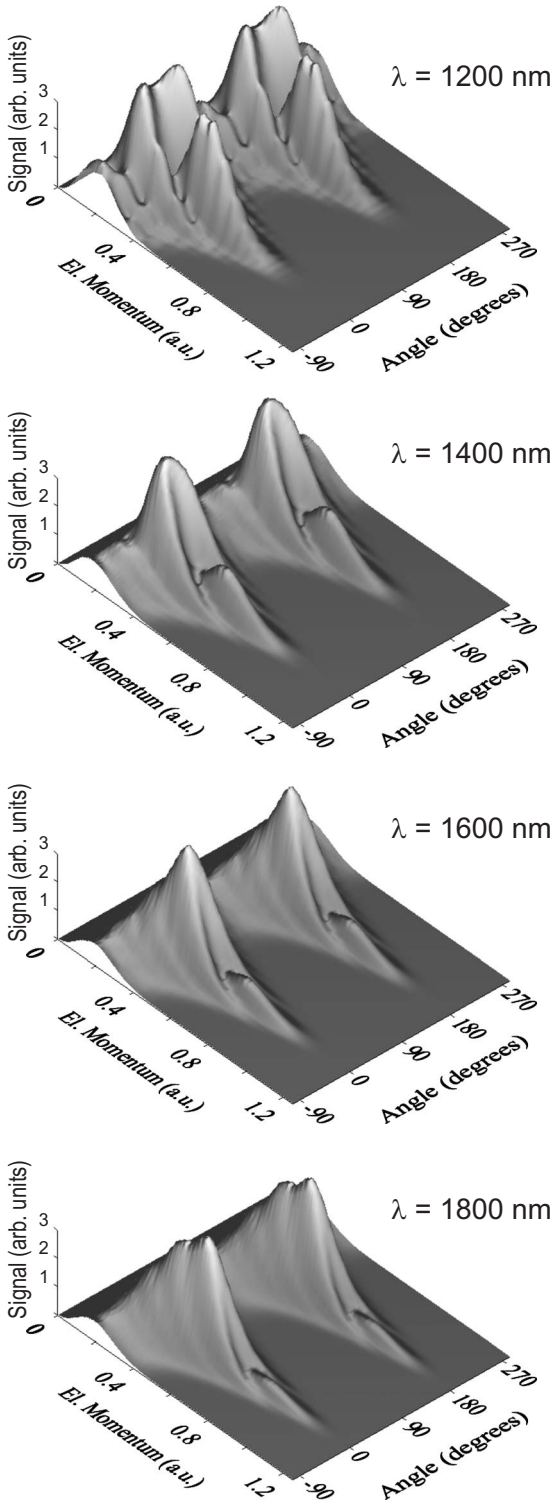

FIG. 6. The wavelength dependence of the photoelectron spectrum at the peak intensity value of 1.7×10^{13} W/cm^2. The wavelength values are given in the figure. The figure shows results of simulations.

of the interference term lies on the exponentially decreasing slope of the amplitude term. Thus, the corresponding maximum of the product of these terms appears at a lower kinetic energy, which makes the agreement with the experimental value even better. One can see from Eq. (15) that with a decrease of the laser frequency the position of the maximum moves towards higher momenta. This is in accordance with the results presented in Fig. 6. The height of the maximum is defined by the amplitude term in Eq. (14). Since this term decreases exponentially with p, the maximum becomes lower while it moves towards higher momenta. From Eq. (14) we also see that the number of oscillations of the interference term in a momentum range between a given finite value p and infinity increases with the decrease of the frequency. It explains the increase of the number of shoulders with the wavelength, as shown in Fig. 6. Indeed, a shoulder (as well as sidelobes) can be assigned to a minimum of the interference term: if at a given momentum the detachment rate at $\theta=0°$ is zero, the emission takes place sideways, forming such a structure in the spectrum.

We would like to emphasize that the analysis presented in this section is rigorous only in the limit of high kinetic energies. It works surprisingly well even when the energy is of the order of $|E_0|$. This differs from the discussion presented in previous sections, where the intensity dependence of the interference pattern is reported at relatively lower kinetic energies.

F. Experimental test of the choice of gauge

In this section we compare our experimental results with predictions of both the length and velocity gauges. The simulation routine in both gauges is the same as described in Sec. III D. The differential n-photon detachment rate in the length gauge is given by Eq. (6). Instead, in the velocity gauge we use the rate equation given by Reiss in Ref. [14]:

$$\frac{dw_n}{d\Omega} = \frac{p}{(2\pi)^2}\left(\frac{p^2}{2} - E_0\right)^2 |\Phi_0(\mathbf{p})|^2 J_n^2\left(\sqrt{\omega}\xi, -\frac{z}{2}\right), \quad (16)$$

where $\Phi_0(\mathbf{p})$ is the Fourier transform of the initial wave function, $J_n(s,q)$ is the generalized Bessel function, and parameters ξ and z are introduced in Eq. (4).

It is worth noting that representation of the wave function by its asymptotic form (7) is, strictly speaking, justified only in the length gauge, where large distances contribute the most to the transition matrix element [6]. Therefore, for simulations in the velocity gauge we use a more precise analytical description of the ground state given by the parametrized Hartree-Fock wave function in the form

$$\Psi_0^{\mathrm{HF}}(\mathbf{r}) = \sum_i C_i N_i r^{n_i - 1} \exp(-\zeta_i r) Y_{\ell m}(\hat{\mathbf{r}}), \quad (17)$$

where the sum involves a finite number of terms and the numerical parameters C_i, N_i, n_i, and ζ_i are given in [30]. In order to test the importance of the initial wave function representation, we performed simulations in the velocity gauge with the use of both the asymptotic and Hartree-Fock wave functions. The difference in the result is found to be small and unessential for the discussion below. One can see from Eq. (16) that the difference is, in fact, defined solely by the factorized Fourier transform term, which can be calculated for both wave functions analytically. In the case of F^- we obtain

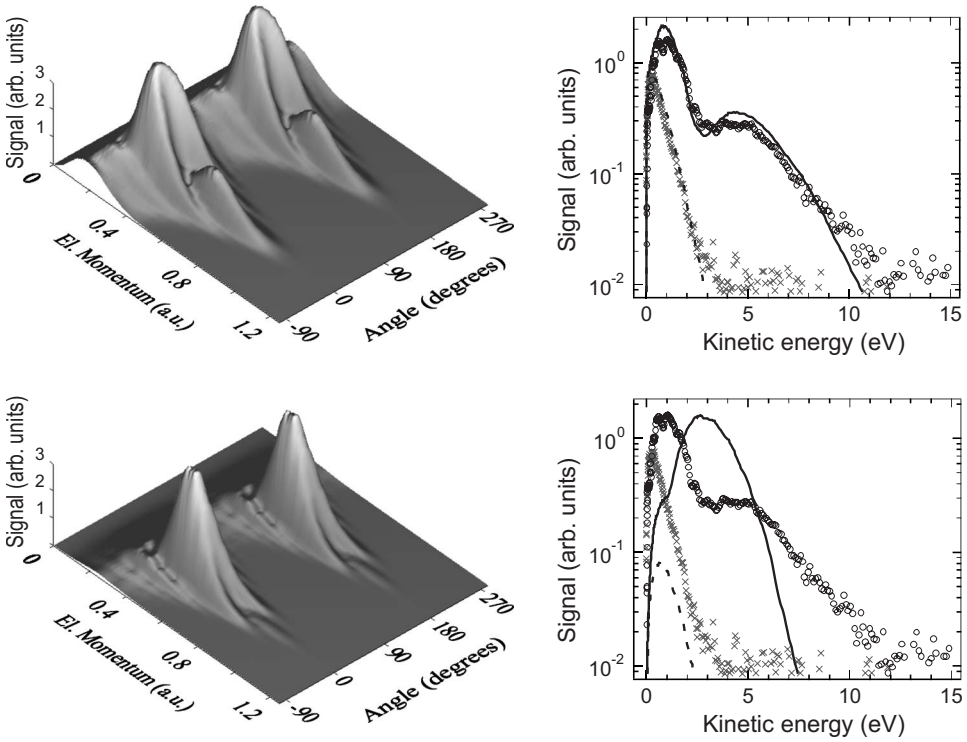

FIG. 7. Photoelectron spectra simulated in the length gauge (top) and in the velocity gauge (bottom) for the peak intensity of 1.7×10^{13} W/cm^2 and the wavelength of 1400 nm. Kinetic energy distributions at 0° and 90° are shown on the right hand side. Notations: solid line, simulated results at 0°; dashed line, simulated results at 90°; circles, experimental results at 0°; crosses, experimental results at 90°. The ratio of the yield at 0° and 90° is conserved in plots shown on the right-hand side.

$$\Phi_0^{\mathrm{A}}(\mathbf{p}) = 4\pi i \frac{C}{p} Y_{1m}(\hat{\mathbf{p}}) \left(\frac{\kappa}{p^2+\kappa^2} - \frac{1}{p} \arctan \frac{p}{\kappa} \right) \qquad (18)$$

for the Fourier transform of the asymptotic wave function (7) and

$$\Phi_0^{\mathrm{HF}}(\mathbf{p}) = -32\pi i Y_{1m}(\hat{\mathbf{p}}) \sum_{i=1}^{4} C_i N_i \frac{\zeta_i p}{(p^2+\zeta_i^2)^3} \qquad (19)$$

for the Fourier transform of the Hartree-Fock wave function (17), where $m=0,\pm1$. Simple calculations show that the ratio $|\Phi_0^{\mathrm{A}}|^2/|\Phi_0^{\mathrm{HF}}|^2$ represents a monotonic function of p that smoothly varies between 1 and 0.3 in the range of electron momenta considered here. As a result, the energetic part of the electron spectrum is more pronounced in calculations with the use of the Hartree-Fock wave function. This difference, however, is of minor absolute value and does not explain the discrepancy between experiment and predictions in the velocity gauge that will be shown below. The calculations presented below in the velocity gauge are carried out with the use of the Hartree-Fock wave function.

Results of simulations in different gauges are shown in Fig. 7 for the 1.7×10^{13} W/cm^2 peak intensity and the 1400 nm wavelength. The calculated data are normalized to the averaged signal in the vicinity of the maximum in the experimental spectrum. Simulations in both gauges exhibit characteristic features attributed to the interference effect. In particular, the nonmonotonic structure that involves sidelobes embracing the second maximum at higher kinetic energies is present in both spectra. The velocity gauge spectrum possesses maxima at higher momenta and is much narrower on the angular scale, as compared to the spectrum simulated in the length gauge. It is evident from Fig. 7 that the length gauge reproduces experimental results (shown in Fig. 2) much better than the velocity gauge.

In order to perform a quantitative comparison of theory and experiment, we plot on the right-hand side of Fig. 7 the measured and simulated energy distributions of photoelectrons emitted at 0° and 90°. The comparison is given separately for the length gauge (upper plot) and the velocity gauge (lower plot). It evidently shows that the length gauge describes experimental data rather well and the velocity gauge fails. In particular, the main maximum in the experimental data at the kinetic energy of 1 eV is not reproduced in the velocity gauge. Instead, in this gauge the main maximum appears at the energy of 3 eV, where the experimental curve has a local minimum and it has a much broader width. The second maximum at the energy of 4.5 eV in the data for the 0° emission angle is well reproduced in the length gauge. In the velocity gauge this maximum has approximately two orders of magnitude lower value and lies below the noise level of approximately 10^{-2} (arbitrary units) in the experimental data. Therefore, it is not shown in the lower plot. From the three-dimensional spectrum on the left-hand side one can also see that the second maximum in the velocity gauge appears at a much higher electron momentum of approximately 0.9 a.u., corresponding to the kinetic energy value of 10 eV. Considering electron emission at the angle of 90°, very good agreement between theory and experiment is found in the length gauge, while a discrepancy of one order of magnitude in the electron yield arises in the velocity gauge. We should note that the ratio of the yield at 0° and 90° is conserved in plots shown on the right-hand side.

In Fig. 8 we show photoelectron angular distributions at three kinetic energies. Their values are chosen in the vicinity of the main peak in the experimental data, in the vicinity of

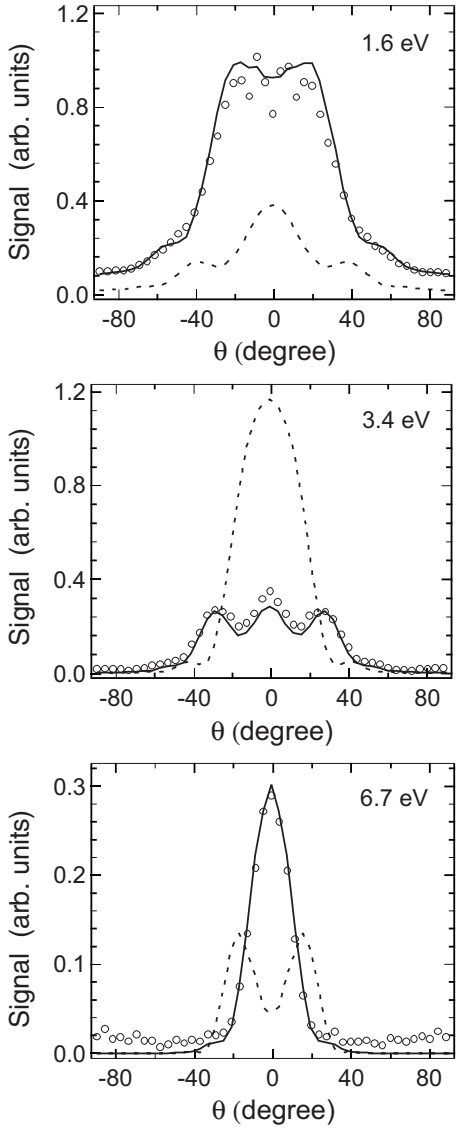

FIG. 8. Photoelectron angular distribution at three values of the kinetic energy: circles, experimental data; solid line, prediction in the length gauge; dashed line, prediction in the velocity gauge. Results are shown for the 1.7×10^{13} W/cm^2 peak intensity and 1400 nm wavelength.

the saddle, and on the slope of the second highest energy peak. Note that we keep the same normalization of curves as in Fig. 7. One can find an excellent agreement between experimental data and predictions in the length gauge. It is also evident from the figure that predictions in the velocity gauge reproduce neither the shape nor the relative heights of angular distributions.

Our experimental results unambiguously indicate that the length gauge should be used in the Keldysh theory. The above discussion demonstrates a large discrepancy in the character of the interference structure predicted in different gauges. This discrepancy should be related to the fact that in the length gauge the interference term is dependent on the angular momentum quantum numbers ℓ and m of the initial state [see Eq. (6)]. On the contrary, in the velocity gauge the interference structure described by the generalized Bessel function is independent of ℓ and m. Such a principal difference results in qualitatively different shapes of electron distributions: a minimum predicted in one gauge coincides with a maximum in another gauge. Our findings support results of the direct numerical integration of the Schrödinger equation [22], where basically the same qualitative discrepancy is found in the case of photodetachment of an odd-parity ground state.

IV. SUMMARY

In this work the study of electron photodetachment of F^- in a strong linearly polarized laser field is extended to a wide range of frequencies and peak intensities. We have demonstrated how the nonmonotonic structure observed in photoelectron spectra emerges from the interference term in Eq. (6). Both the laser frequency and the field strength determine the interference character at lower electron momenta, while in the limit of high momenta and at small emission angles the interference effect becomes independent of the field strength.

The excellent agreement between our measurements and predictions of the Keldysh-like theory by Gribakin and Kuchiev over a wide range of experimental parameters asserts the validity of the strong-field approximation. We have also clearly demonstrated that the length gauge should be used in the description of the electron interaction with the external electromagnetic field. The difference between predictions in the length and velocity gauges lies in the different character of the interference pattern. Maxima of the measured photoelectron distributions arising from constructive interference, as is described in the length gauge, coincide with minima of the velocity gauge predictions. This is related to the fact that the symmetry properties of the ground-state wave function, which determine the interference pattern in the length gauge, do not affect the nonmonotonic character of spectra predicted in the velocity gauge.

ACKNOWLEDGMENTS

The authors greatly appreciate fruitful discussions of this work with Professor Hanspeter Helm. This research is supported by the Deutsche Forschungsgemeinschaft, Grant No. KI 865/1-3. D.H. acknowledges support from the Swedish Research Council.

[1] For references see, e.g., L. F. DiMauro and P. Agostini, Adv. At., Mol., Opt. Phys. **35**, 79 (1995).
[2] M. Saeed, M. J. Dyer, and H. Helm, Phys. Rev. A **49**, 1491 (1994).
[3] K. J. Schafer, B. Yang, L. F. DiMauro, and K. C. Kulander, Phys. Rev. Lett. **70**, 1599 (1993).
[4] P. B. Corkum, Phys. Rev. Lett. **71**, 1994 (1993).
[5] W. Becker, F. Grasbon, R. Kopold, D. B. Milošević, G. G. Paulus, and H. Walther, Adv. At., Mol., Opt. Phys. **48**, 35 (2002).
[6] G. F. Gribakin and M. Yu. Kuchiev, Phys. Rev. A **55**, 3760 (1997).
[7] R. Kopold and W. Becker, J. Phys. B **32**, L419 (1999); R. Kopold, W. Becker, and M. Kleber, Opt. Commun. **179**, 39 (2000).
[8] I. Yu. Kiyan and H. Helm, Phys. Rev. Lett. **90**, 183001 (2003).
[9] P. Hansch, M. A. Walker, and L. D. Van Woerkom, Phys. Rev. A **55**, R2535 (1997).
[10] M. P. Hertlein, P. H. Bucksbaum, and H. G. Muller, J. Phys. B **30**, L197 (1997).
[11] L. V. Keldysh, Sov. Phys. JETP **20**, 1307 (1964).
[12] A. M. Perelomov, V. S. Popov, and M. V. Terent'ev, Sov. Phys. JETP **23**, 924 (1966).
[13] F. H. M. Faisal, J. Phys. B **6**, L89 (1973).
[14] H. R. Reiss, Phys. Rev. A **22**, 1786 (1980).
[15] D. M. Volkov, Z. Phys. **94**, 205 (1935).
[16] R. Reichle, H. Helm, and I. Yu. Kiyan, Phys. Rev. Lett. **87**, 243001 (2001).
[17] B. Bergues, Y. Ni, H. Helm, and I. Yu. Kiyan, Phys. Rev. Lett. **95**, 263002 (2005).
[18] E. P. Wigner, Phys. Rev. **73**, 1002 (1948).
[19] R. Reichle, H. Helm, and I. Yu. Kiyan, Phys. Rev. A **68**, 063404 (2003).
[20] S. Beiser, M. Klaiber, and I. Yu. Kiyan, Phys. Rev. A **70**, 011402(R) (2004).
[21] M. V. Frolov, N. L. Manakov, E. A. Pronin, and A. F. Starace, Phys. Rev. Lett. **91**, 053003 (2003).
[22] D. Bauer, D. B. Milošević, and W. Becker, Phys. Rev. A **72**, 023415 (2005).
[23] A. T. J. B. Eppink and D. H. Parker, Rev. Sci. Instrum. **68**, 3477 (1997).
[24] C. Bordas, F. Paulig, H. Helm, and D. L. Huestis, Rev. Sci. Instrum. **67**, 2257 (1996).
[25] David A. Dahl, computer code SIMION 3D, version 6.0, ASMS, 1995.
[26] V. E. Chernov, I. Yu. Kiyan, H. Helm, and B. A. Zon, Phys. Rev. A **71**, 033410 (2005).
[27] L. D. Landau and E. M. Lifshitz, *Quantum Mechanics. Non-relativistic Theory* (Pergamon, Oxford, 1965).
[28] R. Reichle, I. Yu. Kiyan, and H. Helm, J. Mod. Opt. **50**, 461 (2003).
[29] T. Andersen, H. K. Haugen, and H. Hotop, J. Phys. Chem. Ref. Data **28**, 1511 (1999).
[30] A. A. Radzig and B. M. Smirnov, *Reference Data on Atoms, Molecules, and Ions* (Springer-Verlag, Berlin, 1985).